Off-Design Performance of a Streamline-Traced, External-Compression Supersonic Inlet

John W. Slater
John.W.Slater@nasa.gov
NASA John H. Glenn Research Center at Lewis Field
Inlets and Nozzles Branch, Propulsion Division, Research and Engineering Directorate
Cleveland, Ohio
United States of America

ABSTRACT

A computational study was performed to explore the aerodynamic performance of a streamline-traced, external-compression inlet designed for Mach 1.664 at off-design conditions of freestream Mach number, angle-of-attack, and angle-of-sideslip. Serious degradation of the inlet performance occurred for negative angles-of-attack and angles-of-sideslip greater than 3 degrees. At low subsonic speeds, the swept leading edges of the inlet created a pair of vortices that propagated to the engine face. Increasing the bluntness of the cowl lip showed no real improvement in the inlet performance at the low speeds, but did improve the inlet performance at the design conditions. Reducing the inlet flow rate improved the inlet performance, but at the likely expense of reduced thrust of the propulsion system. Deforming the cowl lip for low-speed operation of the inlet increased the inlet capture area and improved the inlet performance.

Keywords: Supersonic Inlet; Computational Fluid Dynamics; Internal Aerodynamics

NOMENCLATURE

AIP	Aerodynamic Interface Plane
BC	Boundary Condition
IDC	Circumferential distortion index
IDR	Radial distortion index

Symbols

α	Angle-of-attack
β	Angle-of-sideslip
Δs_{ref}	Normalized grid resolution
M_0	Freestream Mach number
M_2	Average AIP Mach number
M_{BC}	Outflow Mach number boundary condition
N	Number of grid points
p_{t0}	Freestream total pressure
p_{t2}	Average AIP total pressure
T_{t0}	Freestream total temperature
W_2	Inlet AIP flow rate
W_{cap}	Capture flow rate
W_{C2}	AIP corrected flow rate
W_{C2*}	Design AIP corrected flow rate
x, y, z	Cartesian coordinates

1.0 INTRODUCTION

The streamline-traced, external-compression (STEX) inlet is being studied as a component of a turbo-fan propulsion system for future commercial supersonic aircraft for flight speeds of about Mach 1.6.[1-5] The STEX inlet has an external supersonic diffuser that is shaped from the tracing of streamlines through a compressive, supersonic parent flowfield.[1,2] The inward-turning nature of the supersonic compression results in near-zero external cowl angles, which significantly reduces the cowl wave drag compared to the wave drag of traditional axisymmetric-spike inlets.[1,3] The leading edge of the inlet is swept (scarfed) rearward. The terminal shock is located near the end of the external supersonic diffuser such that the subsonic spillage past the cowl lip is localized to a small segment of the circumference of the cowl lip. This can allow the inlet to be integrated with the aircraft in such a manner as to control the interaction of the spillage with the aircraft surfaces. The low external cowl angles and localized subsonic spillage also reduce and localize external pressure disturbances that can contribute to sonic boom, which would be beneficial to future commercial supersonic aircraft that will be designed for supersonic flight over populated land regions.[1,4] A computational study was performed in which the STEX inlet was integrated with a low-boom supersonic concept aircraft.[4] It was found that the STEX inlet had a slight reduction in aircraft drag compared to a traditional axisymmetric-spike inlet when integrated with the aircraft. The resulting sonic boom disturbances showed very little difference between the two inlets. One conclusion was that the inlet performance and sonic boom was highly dependent on the integration of the inlet within the entire supersonic aircraft flowfield.[4] A concern with the STEX inlet flowfield was that the total pressure recovery was lower and total pressure distortion was higher in comparisons with an axisymmetric-spike inlet designed for the same conditions as the STEX inlet.[1,3] This was mainly due to a more adverse terminal shock / boundary layer interaction within the STEX inlet. The interaction was followed by a localized outward-turning of the flow into the subsonic diffuser, which created a low-momentum region within the upper surfaces of the subsonic diffuser.[1,3,4] One approach studied for improving the internal flowfield was to introduce porous bleed within the throat section downstream of the terminal shock / boundary layer interaction.[3] Another approach studied was to introduce vortex generators to redistribute the low-momentum flow and reduce total pressure distortion at the AIP.[5] Both approaches yielded acceptable performance for the STEX inlet.

This paper discusses the aerodynamic performance of the STEX inlet of Reference [5] at off-design conditions. Section 2.0 discusses the STEX inlet design. Section 3.0 discusses the computational methods used to design the inlet, model the geometry, generate the computational grid, and solve the flowfield. Section 4.0 discusses the performance of the STEX inlet at the design conditions, at angle-of-attack, at angle-of-sideslip, and at Mach numbers through the subsonic and supersonic range. Section 4.0 continues with a discussion of several approaches for improving the inlet performance at low-speed conditions which include using a blunter cowl lip, reducing the inlet flow rate, and deforming the cowl lip.

2.0 THE STEX INLET

The design of the STEX inlet was performed using the SUPIN (Supersonic Inlet Design and Analysis) tool.[6] SUPIN uses the freestream and AIP conditions along with a small set of design factors to size the inlet, compute the inlet performance, and create the inlet geometry. SUPIN used compressible flow relations, empirical models, and quick computational solutions to estimate the quasi-one-dimensional flow properties through the inlet flowpath. The inlet performance was characterized by the inlet flow rate, total pressure recovery at the AIP, and the cowl wave drag. Cowl wave drag is not examined in this paper. Also, SUPIN does not estimate the total pressure distortion at the AIP, which in this paper is obtained from computational simulations.

The streamline-traced, external-compression (STEX) inlet was designed for a freestream Mach number of M_0 = 1.664, which corresponded to conditions of a potential test within the 8x6-foot supersonic wind tunnel at the NASA Glenn Research Center. The freestream total pressure and total temperature were p_{t0} = 21.535 psi and T_{t0} = 622.5 ^{o}R, respectively. The circular engine face had a diameter of 0.979 feet and included an elliptical spinner with a hub-to-tip ratio of 0.315 and aspect ratio of 2.0. These dimensions of the engine face were scaled from publically-available information for the General Electric F404-GE-400 engine, which powers the F/A-18E/F aircraft and is a suitable engine for a supersonic aircraft. The engine corrected flow rate used for the design corresponded to a mass-averaged Mach number of 0.478 at the engine face. The aerodynamic interface plane (AIP) was located at the engine face. The axisymmetric parent flowfield for the STEX inlet streamline-tracing was established with a Mach 1.664 inflow and a Mach 0.9 outflow using the Otto-ICFA-Busemann method.[2] The internal angle of the leading edge was -5.0 degrees. The parent flowfield contained a weak oblique shock as the leading wave followed by an isentropic supersonic compression that ended with a strong oblique terminal shock that decelerated the flow to Mach 0.9 and turned the flow into the axial direction. The surface of the external supersonic diffuser was created by streamline-tracing in the upstream direction through the parent flowfield starting from a circular tracing curve at the throat. The circular tracing curve was offset from the axis-of-symmetry of the parent flowfield to result in a scarfed leading edge for the external supersonic diffuser. The throat section contained a rounded shoulder to aid the turning of the subsonic flow into the subsonic diffuser. The surface of the external supersonic diffuser and throat was also adjusted radially outward to account for the estimated displacement thickness of the boundary layer expected on the external supersonic diffuser. The throat also featured a "cut-out" at the bottom of the leading edge of the inlet. This "cut-out" created an opening downstream of the terminal shock that allowed subsonic spillage and the smooth positioning of the terminal shock with change in the inlet flow rate.[3] The subsonic diffuser was created to be axisymmetric about the inlet axis, which was coincident with the engine axis. The subsonic diffuser had a length of 2.0 feet that resulted an equivalent conical angle of 2.94 degrees. The STEX inlet had a capture area of 0.597 square-feet and inlet length of 3.353 feet. Figure 1 shows images of the STEX inlet. The total pressure recovery estimated by SUPIN was p_{t2}/p_{t0} = 0.934.

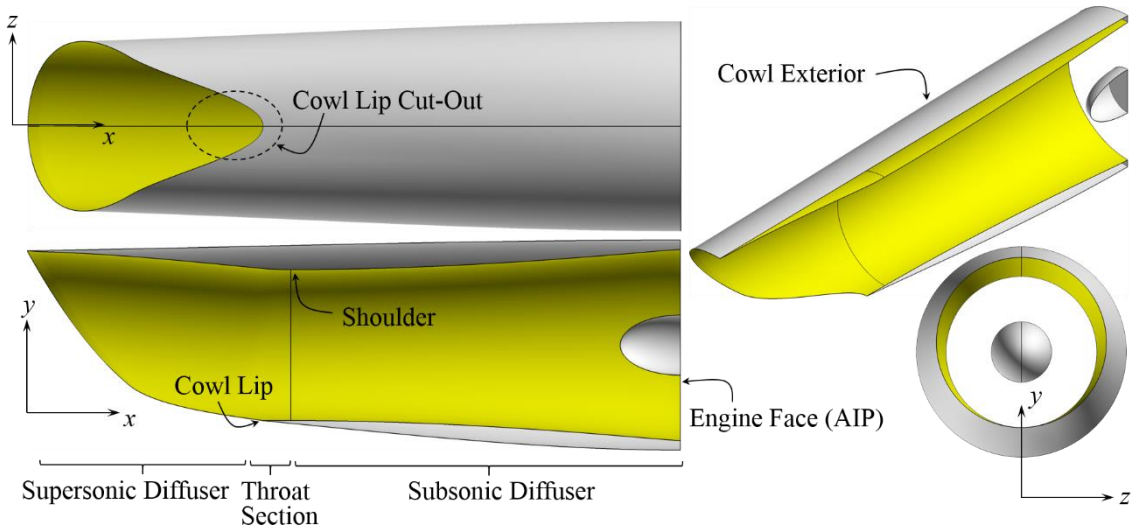

Figure 1. The streamline-traced, external-compression (STEX) inlet.

3.0 COMPUTATIONAL METHODS

While SUPIN was used to design the STEX inlet and provide an initial estimate of the inlet performance, methods of computational fluid dynamics (CFD) were used to perform higher-fidelity analyses of the aerodynamics of the flow through the STEX inlet. The Wind-US CFD code was used to solve the steady-state, Reynolds-Averaged Navier-Stokes (RANS) equations for flow properties on a multi-block, structured grid within the flow domain about the inlet.[7] The CFD solutions allowed visualization of the flowfield to better understand the shock structures, boundary layers, and other flow features within and about the inlet. From the flowfield, the inlet performance metrics were obtained.

Figure 2 shows an example of the flow domain and boundary conditions used for some of the CFD simulations. The flow domain defines the control volume in which the RANS equations are solved. The flow domain shown only includes half of the inlet because geometric and flowfield symmetry about a vertical plane through the inlet was assumed. A flow domain that included the entire inlet was needed for the CFD simulations of the inlet flowfield at angles-of-sideslip. The internal and external surfaces of the inlet formed a portion of the boundary of the flow domain where non-slip, adiabatic viscous wall boundary conditions were imposed. The inflow and farfield boundaries of the flow domain had freestream boundary conditions imposed in which the Mach number, pressure, temperature, angle-of-attack, and angle-of-sideslip were specified. For supersonic freestream conditions, the inflow and farfield boundaries were positioned just upstream of the leading edge oblique shock. For subsonic freestream conditions, the inflow and farfield boundaries were moved away from the inlet surfaces a distance of four AIP diameters. At the end of the cowl exterior, the domain had an external outflow boundary where an extrapolation boundary condition was applied for supersonic outflow and freestream conditions applied for subsonic outflow.

Downstream of the engine face (AIP), an outflow nozzle section was added to the flow domain to set the flow rate within the inlet. The nozzle section moved the internal outflow boundary condition downstream of the AIP by two AIP diameters to reduce any possible interference of the flow at the AIP due to the methods used to impose the internal outflow boundary condition. A couple approaches were used to specify the internal outflow boundary condition. The first approach was to generate a converging-diverging nozzle with a choked throat, as shown in Fig. 2. This created a non-reflective, supersonic condition at the internal outflow boundary for which an extrapolation boundary condition was applied. The inlet flow rate was set by the cross-sectional area of the nozzle throat. The second approach was to generate a constant-area outflow nozzle and impose a subsonic outflow condition at the internal outflow boundary. In this approach, the subsonic Mach number (M_{BC}) was specified as the boundary condition. Both approaches were used in this work and should result in the same steady-state solution for consistent conditions. The discussions of Section 4.0 indicate which approach was used.

The multi-block, structured grids were generated for the flow domain using SUPIN. SUPIN used inputs to define the grid spacing normal to the wall, streamwise grid spacing within the throat section, and grid spacing normal in the cross-stream direction. This established the number of grid points along the edges and surfaces of the inlet and within the flow domain. SUPIN also created the boundary condition file for Wind-US.

Wind-US used a cell-vertex, finite-volume representation for which the flow solution was located at the grid points. In Wind-US, the RANS equations were solved for the steady-state flow solution using an implicit time-marching algorithm with a first-order, implicit Euler method using local time-stepping.[7] The flowfield was initialized at all grid points with the freestream conditions. A calorically-perfect air model was used. The inviscid fluxes of the RANS equations were modeled using a second-order, upwind Roe flux-difference splitting method. The flow was assumed to be fully turbulent with the turbulent eddy viscosity calculated using the two-equation Menter shear-stress transport (SST) model.

Iterative convergence of each solution was evaluated through monitoring convergence of the inlet flow rate, total pressure recovery and distortion. The steady-state solution was considered converged when these values varied less than 0.1% of their values over hundreds of iterations. The solution residuals were also monitored to check that they reduced and approached steady-state values. Grid convergence was examined by computing the flow solution on a series of grids with varying grid resolutions. The grid convergence will be discussed in Section 4.1.

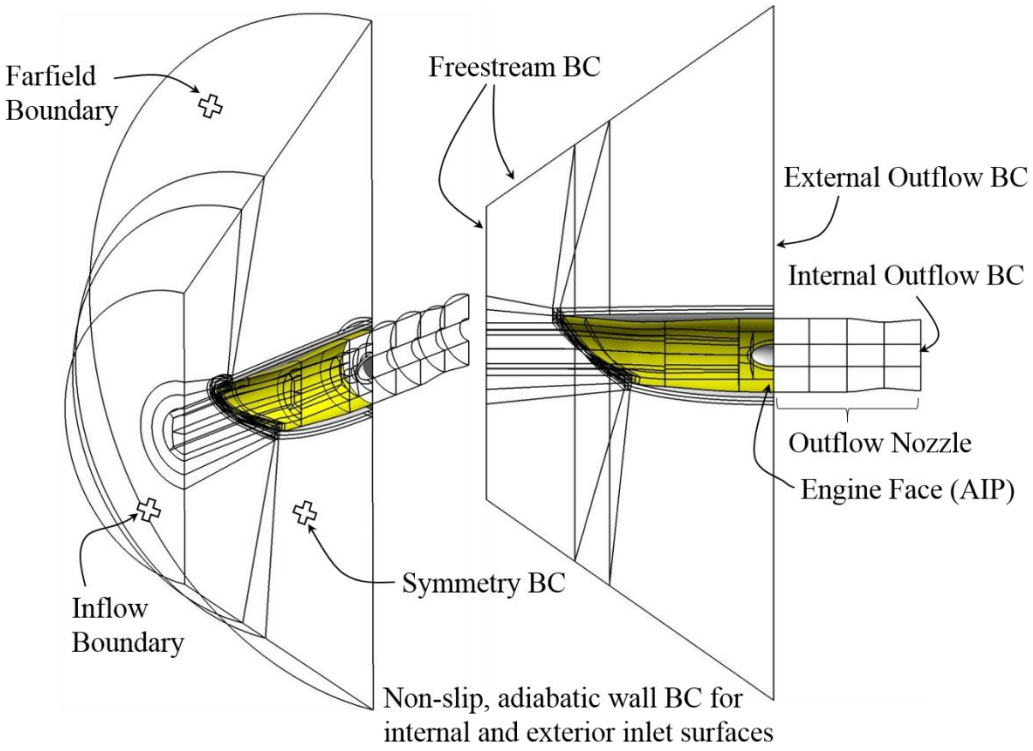

Figure 2. The flow domain and boundary conditions for some of the CFD simulations of the STEX inlet.

4.0 RESULTS

This section first presents the performance of the inlet at the design conditions of M_0 =1.664, 0 degrees angle-of-attack, and 0 degrees angle-of-sideslip. The second and third sub-sections present the inlet performance at angles-of-attack and angles-of-sideslip, respectively, at the design Mach number. The fourth sub-section presents the inlet performance for off-design freestream Mach numbers as low as M_0 = 0.2. The last sub-section examines approaches for improving the inlet performance at low-speed conditions.

4.1 STEX Inlet Performance at the Design Conditions

This section discusses the performance of the inlet at the design Mach number. Included is a discussion of the grid convergence of the computational simulation. The first metric of inlet performance was the inlet flow ratio, which was defined as the rate of flow passing through the AIP divided by the reference capture flow rate (W_2/W_{cap}). The inlet flow rate (W_2) was computed from the simulation as the average of the flow through each of the axial grid surfaces through the outflow nozzle section. At the critical inlet flow rate, the inlet flow rate is equal to the reference capture flow rate ($W_2 = W_{cap}$) and the terminal shock is located at the cowl lip plane. The middle row of images of Fig. 3 shows the inlet flowfield near the critical operating condition. The left column of images shows the Mach number contours on the symmetry plane of the inlet. The Mach number contours show the oblique shock originating at the top leading edge and passing ahead of the cowl lip. The terminal shock is shown in the region of the cowl lip and extends to the top surface of the inlet interior ahead of the shoulder. The middle column shows the Mach number contours at the AIP. Only half of the AIP is shown because the flow domain included only half of the inlet. The right column shows the total pressure recovery contours at the AIP. The interaction of the terminal shock with the boundary layer of the external supersonic diffuser creates a low-momentum region along the top of the throat section and subsonic diffuser.

At supersonic freestream conditions, the inlet flow rate cannot exceed the reference capture flow. Thus, increasing the nozzle throat area beyond that for the critical flow condition will only draw the terminal shock into the inlet to create a supercritical condition. The bottom row of images of Fig. 3 shows the inlet at a supercritical operating condition. For the supercritical operating condition, the terminal shock was drawn slightly into the inlet with a pocket of higher Mach number flow ahead of the shoulder. This resulted in a stronger terminal shock, which resulted in a larger region of low-momentum flow at the top surface of the subsonic diffuser.

Reducing the nozzle throat area below that for the critical flow condition will reduce the inlet flow rate and increase the back-pressure in the subsonic diffuser to create a subcritical condition. The top row of images of Fig. 3 shows the inlet at a subcritical operating condition. The terminal shock was pushed forward on the external

supersonic diffuser as the increased excess inlet flow was spilled past the cowl lip. The region of low-momentum flow is smaller for the subcritical condition than that of the critical condition. This likely reflects the position of the terminal shock forward of the shoulder where there is less curvature of the surface.

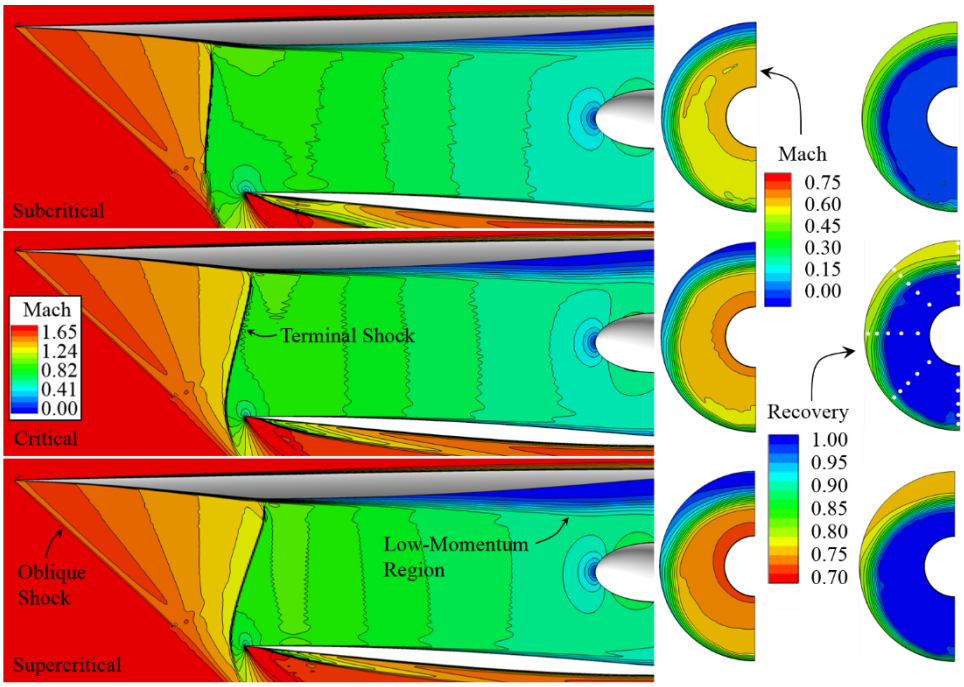

Figure 3. The left column shows the Mach number contours on the symmetry plane of the inlet from the CFD simulations for subcritical (top row), critical (middle row), and supercritical (bottom row) flow conditions. The middle and right columns show the Mach number and total pressure recovery contours, respectively, at the AIP.

The second metric of inlet performance was the inlet total pressure recovery, which was calculated as the mass-averaged total pressure at the AIP divided by the freestream total pressure (p_{t2}/p_{t0}). The variation of the inlet total pressure recovery with the inlet flow ratio creates the inlet characteristic curve, which is also known as the "cane" curve because of its resemblance to a walking cane. Figure 4 shows three characteristic curves for the STEX inlet at the design Mach number. The three characteristic curves correspond to three grids of varying refinement used to evaluate the grid convergence of the inlet flowfield simulations. Grid 0 is the coarsest grid and Grid 2 is the finest grid. The grid convergence will be discussed in greater detail later in this section. The bend of the curve is the "knee" and represents the conditions near critical flow. The segment of the curve for the supercritical conditions is the nearly vertical segment below the "knee" and indicates nearly constant inlet flow ratio. The segment of the curve for the subcritical conditions to the left of the "knee" indicate gradually lower inlet flow ratios as more flow is spilled past the cowl lip. The total pressure recovery decreases with lower inlet flow ratio, which indicates the terminal shock encounters higher Mach number flow on the external supersonic diffuser.

The third and fourth metrics of inlet performance were descriptors of the circumferential and radial total pressure distortion at the AIP as represented by the IDC and IDR distortion descriptors, respectively. The IDC and IDR distortion descriptors were defined by General Electric.[8] The IDR radial distortion descriptor was computed in the same manner as the radial distortion descriptor defined in the SAE Aerospace Recommended Practices (ARP) 1420 document.[9] The IDC circumferential distortion descriptor was computed slightly different than the circumferential distortion descriptor of the SAE ARP 1420 and was generally a higher value than the circumferential distortion descriptor of SAE ARP 1420. The IDC and IDR distortion descriptors were computed from total pressures interpolated from the CFD simulation onto the probe locations of a virtual 40-probe rake as defined according to the SAE ARP 1420. The rake consisted of eight arms or rakes with five probes per rake. The probes were positioned along each rake such that their radial position was at the centroid of equal areas of the annular disk at the AIP. The locations of the probes are shown as the white circles in the middle image of the total pressure recovery contours of Fig. 3. Shown are the five rakes that were used for the half of the AIP. The right image of Fig. 4 shows the plot of IDR and IDC distortion descriptors. Also plotted in Fig. 4 are the limits on IDR and IDC for the F404-GE-400 engine, as obtained from Ref. 10. For IDC < 0.05, the limit on IDR was reduced due to instances of flutter of the F404-GE-400 fan blades observed during aeromechanical testing with radial distortion patterns. As shown in the right-hand-side plot of Fig. 4, the values of the IDR distortion descriptor slightly exceed the radial distortion limit. Ideally, one would like the IDR values at all conditions to be

comfortably within the limit; however, driving the values of IDR and IDC toward zero is not necessary. The high values of IDR corresponded to the low-momentum region that formed at the top of the AIP. The approach for reducing IDR has involved introducing vortex generators into the inlet in such a manner as to distribute the low-momentum region more uniformly about the circumference of the AIP. Reference 5 discusses the design of the vortex generators for the STEX inlet. For the current paper, vortex generators were not used and the off-design performance of the STEX inlet was explored in relation to the on-design performance as summarized in Fig. 4.

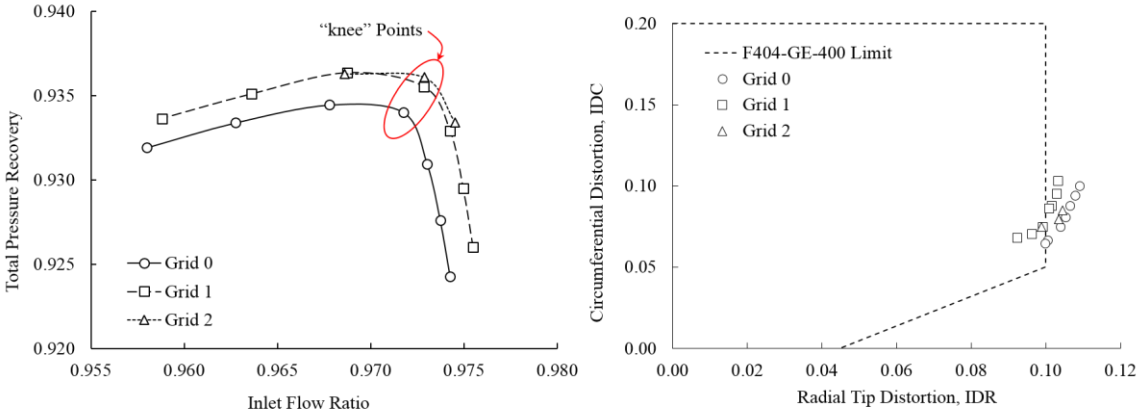

Figure 4. Characteristic curves and distortion indices for the STEX inlet at the design conditions.

The plots of Fig. 4 show results for three grids as part of the examination of the grid convergence of the flowfield simulation of the STEX inlet. Grid 0 is the coarsest grid and Grid 2 is the finest grid. The resolution of a grid is characterized by a reference grid spacing Δs_{ref}, which is the streamwise grid spacing in the throat section of the inlet. Grid 2 used a throat section grid spacing of $\Delta s_{ref} = 0.005$ ft. The circumferential grid spacing in the throat section was twice the streamwise grid spacing. The spacing of the first point off the wall in the throat section for Grid 2 was 0.00001 ft, which yielded a $y+$ value of less than 1. Table 1 summarizes the grid spacing and the resulting numbers of grid points within the interior duct of the inlet. The column labelled Δs_{ref}^* indicates the reference grid spacing normalized by the grid spacing used for Grid 2. The column labelled N_{axial} indicates the number of grid points in the axial direction within the throat section and subsonic diffuser. The column labelled N_{cross} indicates the number of grid points in the direction from the bottom to top of the throat section and subsonic diffuser on the symmetry boundary. The column labelled N_{circum} indicates the number of grid points about the circumference of the throat section and subsonic diffuser.

The plot of the characteristic curves on the left-hand side of Fig. 4 indicate a noticeable difference in the curves with refinement from Grid 0 and Grid 1. The curve of Grid 2 follows closely to the curve of Grid 1. This suggests that the grid convergence of the inlet flow ratio and total pressure recovery has been achieved with Grid 1. Table 1 lists the values of inlet flow ratio and total pressure recovery for the three grids at the knee points near the critical operation of the inlet. The last row of Table 1 lists a percentage indicating the variation between the values of the three grids. This variation is computed as the standard deviation of the three values normalized by the value on Grid 2. As can be seen, the variation for the inlet flow ratio and total pressure recovery is rather small at 0.07% and 0.11%, respectively. Another observation is that as the grid is refined, the total pressure recovery tends to increase. This is consistent with other CFD simulations of inlets.[1,3,5]

The plot of the IDR and IDC distortion descriptors on the right-hand-side of Fig. 4 show that between Grids 0 and 1, the values of IDR decrease. However, the values of IDR for Grid 2 fall between those of Grid 0 and 1. This indicates a greater level of uncertainty in the grid convergence for IDR and IDC on the grids. The variation of the three values at the knee point for IDR and IDC are 2.19% and 4.61%, respectively. It was decided to use Grid 1 for the remaining CFD simulations discussed in the sub-sections below. The variations of the performance metrics listed in Table 1 provide some indication of the uncertainty of the performance metrics with respect to the grid convergence.

Table 1
Inlet performance at the design conditions with critical inlet operation for three levels of grid refinement.

Grid	Δs_{ref}^*	N_{axial}	N_{cross}	N_{circum}	W_2/W_{cap}	p_{t2}/p_{t0}	**IDC**	**IDR**
Grid 0	1.581	422	207	157	0.9717	0.93400	0.0805	0.1053
Grid 1	1.275	504	234	189	0.9729	0.93552	0.0862	0.1008
Grid 2	1.000	550	296	309	0.9729	0.93607	0.0793	0.1035
Variation (%)					0.07%	0.11%	4.61%	2.19%

4.2 STEX Inlet at Angles-of-Attack

This sub-section examines the performance of the STEX inlet at the design Mach number with variation of the angle-of-attack. Grid 1 was used for the CFD simulations. The simulations were performed with the throat area of the outflow nozzle set to that used for the critical flow simulation of Fig. 3. Figure 5 shows images of the inlet flowfields for angles-of-attack between α = -4.0 and +4.0 degrees. The left column of images shows the Mach number contours on the symmetry plane of the inlet. The middle column of images shows the Mach number contours at constant-x (axial) stations through the inlet. The right column of images shows the contours of total pressure recovery at the AIP. Table 2 lists the performance metrics for each angle-of-attack. Table 2 includes the corrected flow rate at the AIP normalized by the design corrected flow rate. This normalized corrected flow rate varied by ±2% over the variation from α = -4.0 to +4.0 degrees. Ideally, one would want this normalized flow rate to be constant over the angle-of-attack variation. Nonetheless, some observations can be noted. At negative angles-of-attack, the leading edge oblique shock was weaker and the Mach numbers ahead of the terminal shock were increased. The terminal shock moved closer to the cowl lip and the terminal-shock / boundary-layer interactions were more severe and resulted in a larger low-momentum region at the top of the subsonic diffuser. Degradation of all performance metrics was observed for the negative angles-of-attack. At the positive angles-of-attack, the leading edge oblique shock was stronger, and so, the Mach numbers ahead of the terminal shock were reduced and the terminal shock moved forward on the external supersonic diffuser. Some of the performance metrics actually improved with the smaller positive angles-of-attack of +1.0 and +2.0 degrees. At the angle-of-attack of +4.0 degrees, there was only a slight degradation of the total pressure recovery and radial distortion, IDR, compared to the angle-of-attack of -4.0 degrees. At the angle-of-attack of +4.0 degrees, a vortex is generated along the leading edge of the inlet downstream of the terminal shock. This vortex continues down into the inlet and appears at the bottom of the AIP.

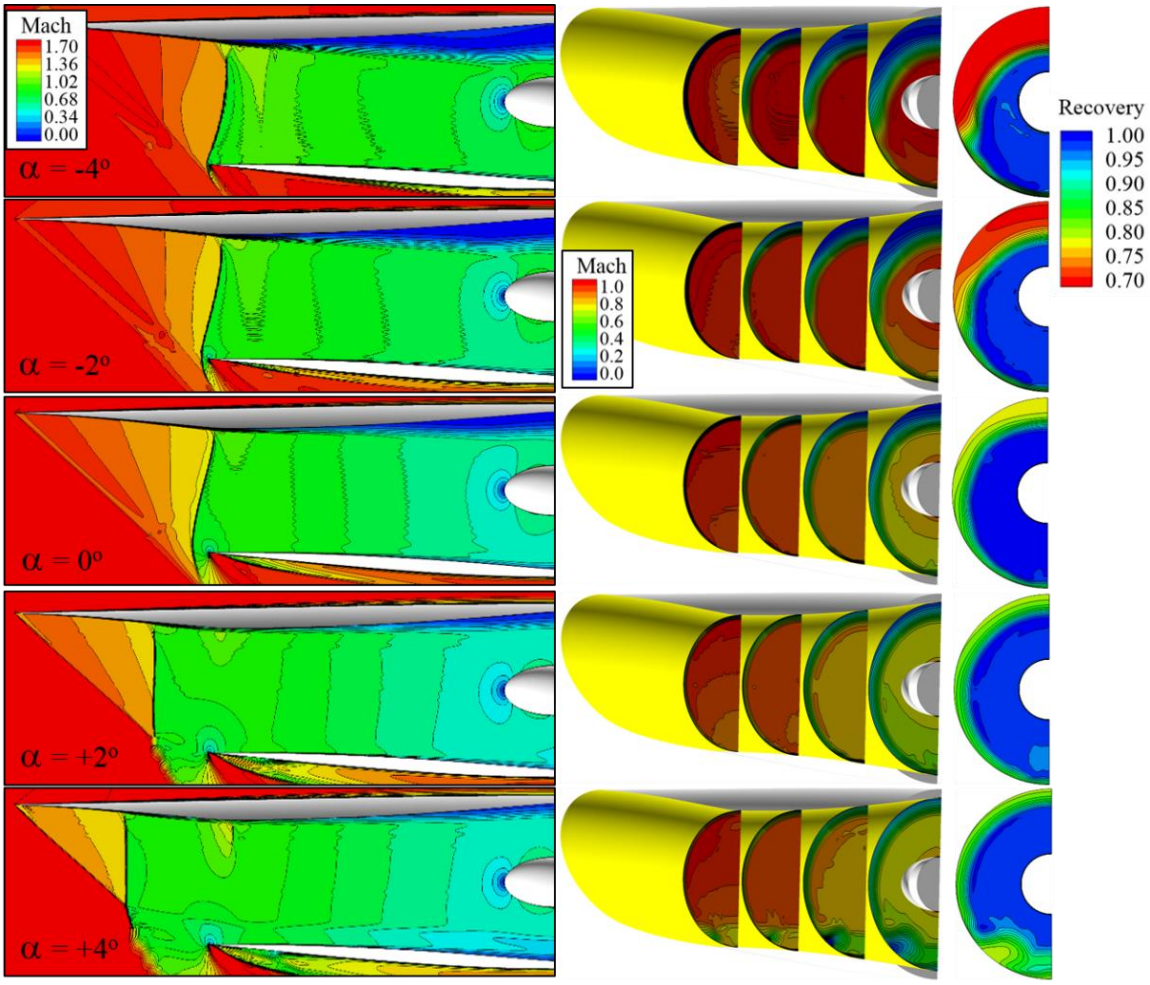

Figure 5. Mach number and AIP total pressure contours at M_0 = 1.664 with variation of the angle-of-attack.

Table 2
Inlet performance metrics at M_0 = 1.664 with variation of the angle-of-attack.

α	W_{C2}/W_{C2^*}	W_2/W_{cap}	p_{t2}/p_{t0}	IDC	IDR
-4.0°	1.0037	0.9035	0.8545	0.1374	0.1048
-3.0°	1.0007	0.9220	0.8746	0.1270	0.1000
-2.0°	0.9972	0.9401	0.8949	0.1163	0.1000
-1.0°	0.9927	0.9576	0.9157	0.1052	0.0987
0.0°	**0.9872**	**0.9729**	**0.9355**	**0.0862**	**0.1008**
+1.0°	0.9822	0.9706	0.9381	0.0618	0.0963
+2.0°	0.9808	0.9699	0.9386	0.0524	0.0933
+3.0°	0.9810	0.9636	0.9325	0.0338	0.1053
+4.0°	0.9814	0.9601	0.9287	0.0411	0.1022

4.3 STEX Inlet at Angles-of-Sideslip

This sub-section examines the performance of the STEX inlet at M_0 = 1.644 with variations of the angle-of-sideslip. Figure 6 shows images of the inlet flow for angles-of-sideslip up to β = +4.0 degrees. Table 3 lists the performance metrics for each angle-of-sideslip. As with the simulations at angle-of-attack, the simulations at angle-of-sideslip were performed with the throat area of the outflow nozzle set to that used for the critical flow simulation of Fig. 3. Since the flow at an angle-of-sideslip was asymmetric, both halves of the inlet about the plane-of-symmetry were included in the computational flow domain. For angles-of-sideslip up to β = +3.0 degrees, there was only a slight degradation of the inlet performance metrics compared to the performance at β = 0.0 degrees. The IDC distortion descriptor decreases with the increase in angle-of-sideslip up to β = +3.0 degrees. The images of the total pressure contours at the AIP show that the low-momentum region along the top of the AIP is more evenly distributed about the circumference of the AIP with increasing angle-of-sideslip. At an angle-of-sideslip of β = +4.0 degrees, the flow past the leading edge on the wind-ward side experienced the dramatic creation of a vortex that propagated to the AIP. The vortex interacted with the boundary layer to result in a large region of low-momentum, circulating flow at the AIP. This greatly increased the IDC distortion descriptor compared to an angle-of-sideslip of β = +3.0 degrees. In addition, the inlet flow rate was reduced and the terminal shock was pushed forward on the external supersonic diffuser. Downstream of the terminal shock, the subsonic flow was reaccelerated and a second, smaller normal shock formed. The total pressure recovery decreased due to the greater losses through the shocks and increased viscous dissipation within the boundary layers.

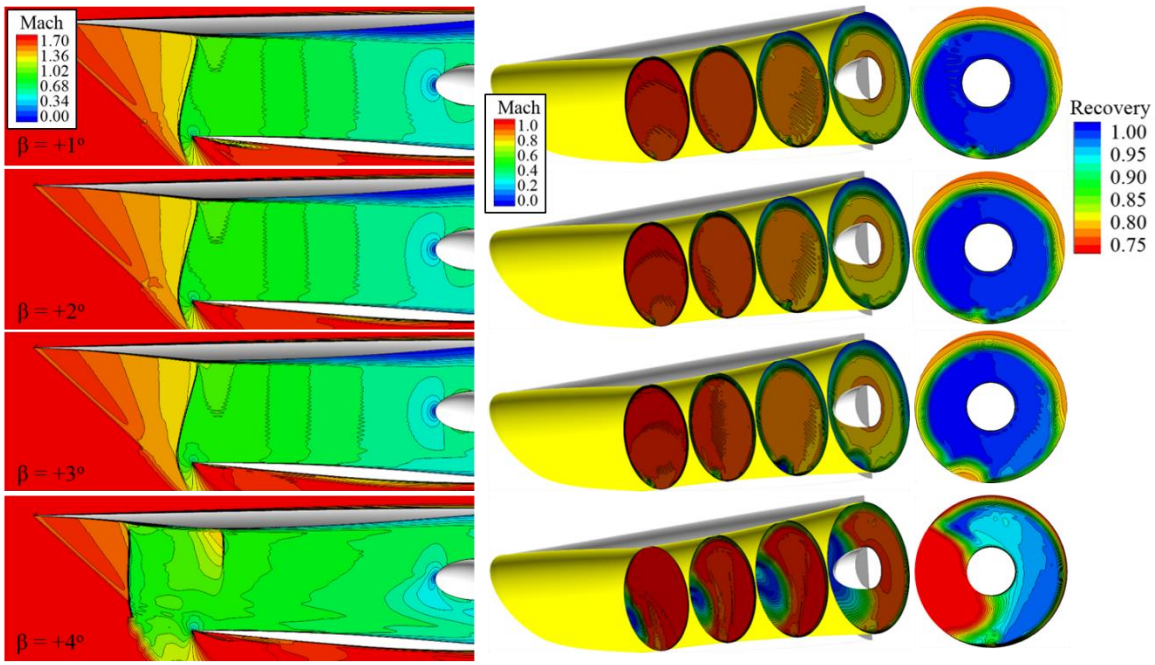

Figure 6. Mach number and AIP total pressure contours at M_0 = 1.664 with variation of the angle-of-sideslip.

Table 3
Inlet performance metrics at M_0 = 1.664 with variation in the angle-of-sideslip.

β	W_{C2}/W_{C2^*}	W_2/W_{cap}	p_{t2}/p_{t0}	IDC	IDR
0.0°	**0.9872**	**0.9729**	**0.9355**	**0.0862**	**0.1008**
1.0°	0.9874	0.9719	0.9343	0.0834	0.1059
2.0°	0.9877	0.9708	0.9330	0.0760	0.1054
3.0°	0.9880	0.9685	0.9306	0.0645	0.1082
4.0°	0.9934	0.8965	0.8567	0.1769	0.0666

4.4 STEX Inlet Performance at Off-Design Mach Numbers

This sub-section examines the performance of the STEX inlet at off-design freestream Mach numbers less than the design Mach number with the lowest Mach number being M_0 = 0.20. For < 0.8, the freestream pressure and temperature were set to be consistent with lower altitudes expected for low-speed operation of the inlet, such as for take-off, climb, and landing. The Mach number outflow boundary condition (M_{BC}) was used to set the AIP corrected flow rate for the CFD simulations at each freestream Mach number consistent with M_2 = 0.478, which corresponded to the design AIP corrected flow rate.

Figure 7 shows the Mach number contours at the symmetry plane and at axial stations through the duct and total pressure recovery contours at the AIP for several supersonic freestream Mach numbers. Figure 8 shows similar images for several subsonic freestream Mach numbers. Figure 9 shows plots of the inlet performance metrics with variation in the freestream Mach number. Table 4 lists the inlet performance metrics for each of the freestream Mach numbers simulated.

As the supersonic freestream Mach numbers decrease, the terminal shock moves forward on the external supersonic diffuser, as shown in Fig. 7, until it disappears for M_0 = 1.0, as shown in Fig. 8. A second shock forms in the throat section as the flow is re-accelerated within the throat. As the freestream Mach number decreased from M_0 = 1.664 to M_0 = 0.8, the total pressure recovery and distortion improved and the flow through the subsonic duct showed little sign of degradation, as shown in Fig. 9 and listed in Table 4.

For freestream Mach numbers of $M_0 \leq 0.6$, the inlet flow ratio began to approach and exceed one, which meant that the inlet streamtube cross-sectional decreased as it flowed past the leading edges of the inlet. The swept or scarfed nature of the leading edges led to the formation of vortices about the leading edge that propagated down the inlet to the AIP. As the freestream Mach number decreased, the intensity and scale of the vortices increased, while the total pressure recovery decreased. The total pressure distortion worsened and changed from a tip distortion to a hub distortion. At Mach 0.2, the vortices grew to engulf over half of the AIP, as shown in Fig. 8. Similar flow features were noted in Ref. [11], which examined the flowfield about a streamline-traced inlet at low-speed conditions.

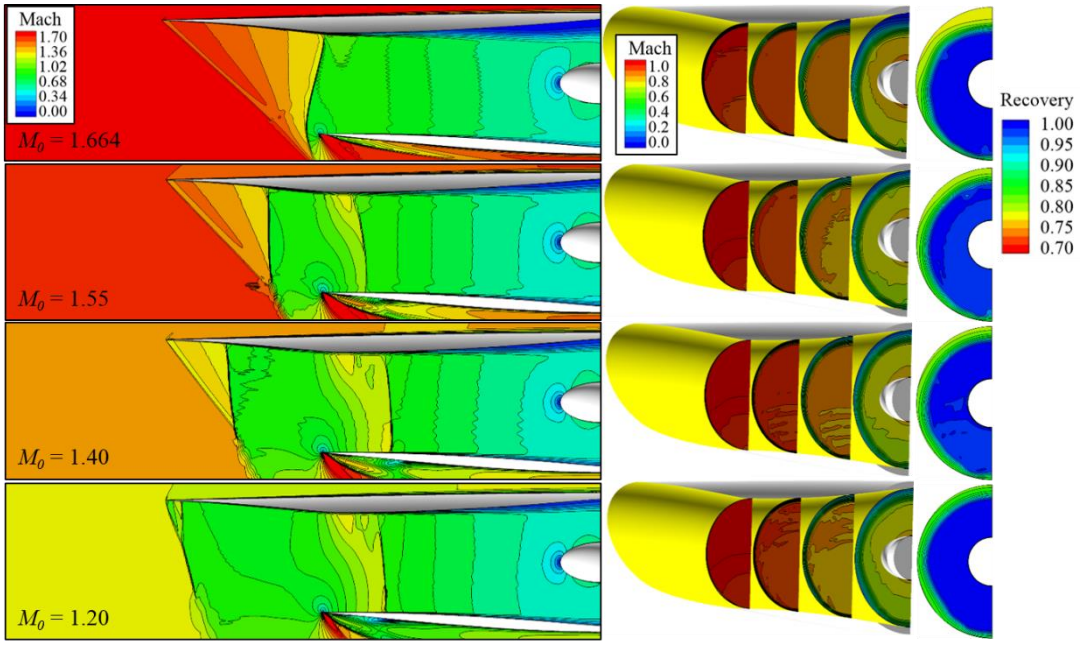

Figure 7. Mach number and AIP total pressure contours over a range of supersonic Mach numbers.

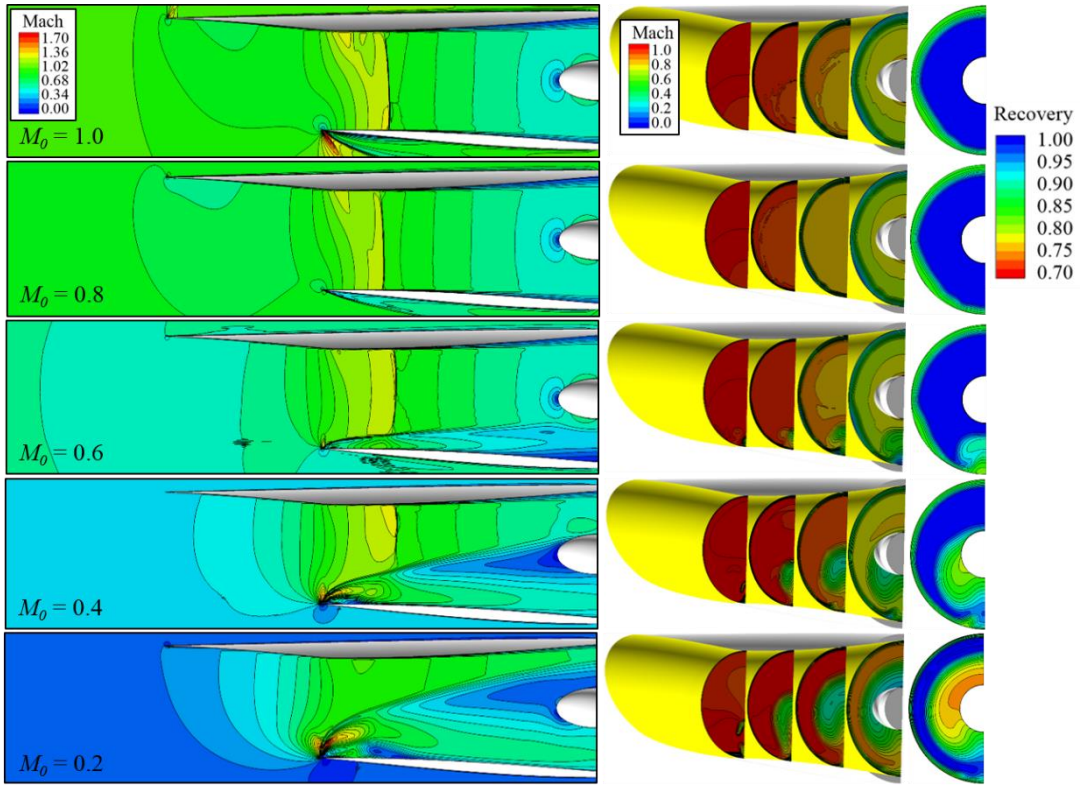

Figure 8. Mach number and AIP total pressure contours over a range of subsonic Mach numbers.

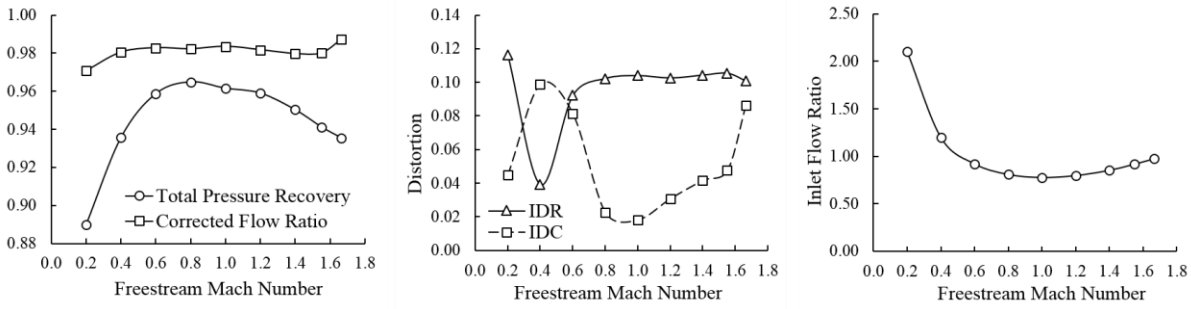

Figure 9. Inlet performance metrics with variation of the freestream Mach number.

Table 4
Inlet performance metrics with variation of the freestream Mach number.

M_0	W_{C2}/W_{C2^*}	W_2/W_{cap}	p_{t2}/p_{t0}	IDC	IDR
1.644	**0.9688**	**0.9696**	**0.9344**	**0.0603**	**0.1111**
1.55	0.9800	0.9176	0.9413	0.0476	0.1054
1.40	0.9797	0.8522	0.9503	0.0417	0.1043
1.20	0.9817	0.7965	0.9590	0.0308	0.1026
1.00	0.9835	0.7764	0.9615	0.0182	0.1040
0.80	0.9822	0.8078	0.9649	0.0227	0.1023
0.60	0.9828	0.9191	0.9587	0.0813	0.0922
0.40	0.9805	1.1976	0.9356	0.0988	0.0391
0.20	0.9707	2.1018	0.8899	0.0448	0.1163

4.5 Modifications to the STEX Inlet to Improve the Performance at Low-Speed Conditions

This sub-section examines modifications of the STEX inlet to improve the inlet performance at low-speed conditions. Each modification and its effect are discussed in the sub-sections below.

4.5.1 Increasing the Bluntness of the Cowl Lip

The STEX inlet has an essentially sharp cowl lip consisting of an elliptical profile with a minor axis length of 0.001 feet at the symmetry plane. At low-speed conditions, the inlet flow ratio is greater than one and the flow entering the inlet must turn past the cowl lip. It was felt that if the cowl lip was made blunter, it would provide greater curvature and length for the flow to negotiate past the cowl lip, and so, reduce the circulating flow region downstream of the cowl lip. This cowl lip was made blunter by using a circular profile and setting its diameter as 0.016 feet. The difference in the bluntness of the cowl lip can be seen in Fig. 10. The profile of the sharp cowl lip at the symmetry plane is shown as an outline while the blunt cowl lip is shown as an outline with a shaded surface.

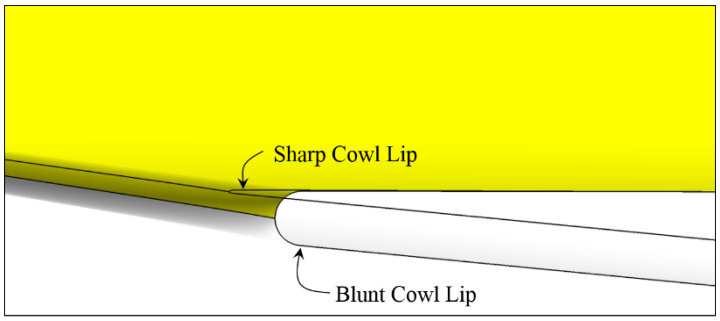

Figure 10. Sharp cowl lip shown as an outline at the symmetry plane along with the blunt cowl lip shown as an outline and shaded image.

CFD Simulations were performed at M_0 = 1.664 to check if the blunt cowl lip adversely affected the inlet performance at the design conditions. Figure 11 shows the Mach number contours at axial stations within the inlets and the total pressure contours at the AIP for both the sharp and blunt cowl lips at M_0 = 1.664. A slight decrease in the extent of the low-momentum flow at the top of the AIP is observed. Figure 12 shows the characteristic curves for the both inlets. The characteristic curve for the inlet with the blunt cowl lip shows an increase in the inlet total pressure recovery with an increase the inlet flow ratio, which is an improvement over the inlet with the sharp cowl lip. Table 5 lists the inlet performance metrics near the design corrected flow rate. At M_0 = 1.664, all of the performance metrics improved for the inlet with the blunt cowl lip compared to the inlet with the sharp cowl lip.

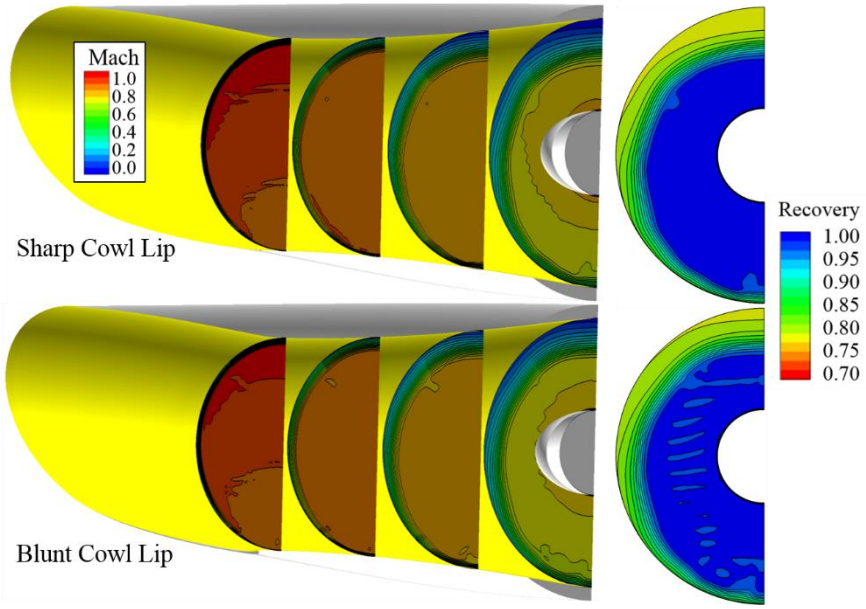

Figure 11. Mach number and AIP total pressure contours at M_0 = 1.664 with sharp and blunt cowl lips.

CFD simulations were performed at M_0 = 0.2 to see whether the inlet performance improved for the inlet with the blunt cowl lip compared to the inlet with the sharp cowl lip. Figure 13 shows the Mach number contours at axial stations within the inlets and the total pressure contours at the AIP for both the sharp and blunt cowl lips at M_0 = 0.2. The images of Fig. 13 do not indicate much of a difference. The values of Table 5 do indicate a slight

improvement in the total pressure recovery and IDC distortion descriptor for the inlet with the blunt cowl lip compared to the inlet with the sharp cowl lip.

While the inlet with the blunt cowl lip did not seem to improve the flow at the low-speed condition, the improvement in the inlet performance at the design conditions suggests that the blunt cowl lip would be a good modification for the STEX inlet.

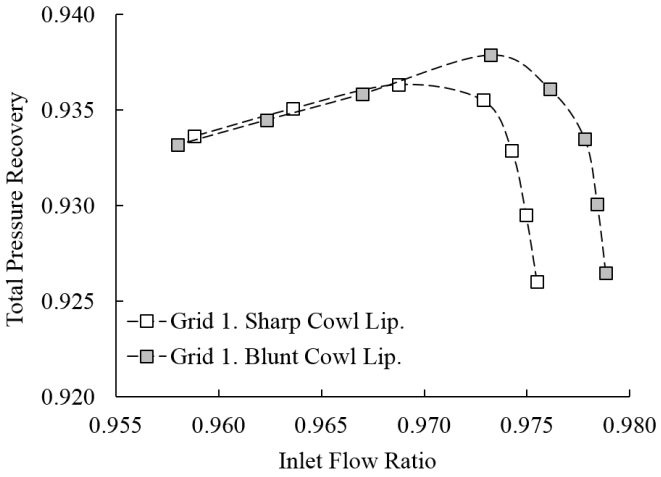

Figure 12. Characteristic curves at M_0 = 1.664 with the sharp and blunt cowl lips.

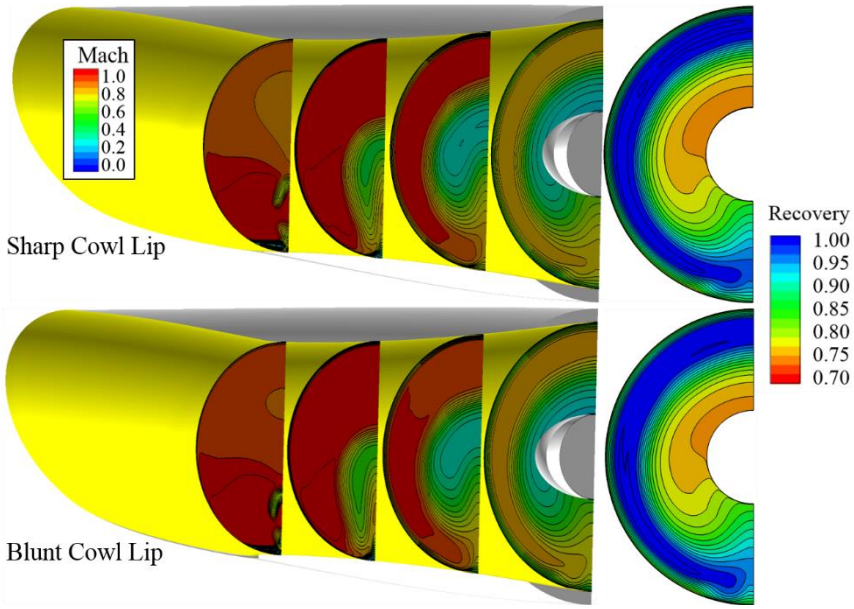

Figure 13. Mach number and AIP total pressure contours at M_0 = 0.2 with sharp and blunt cowl lips.

Table 5
Inlet performance metrics at M_0= 1.664 and M_0= 0.2 with sharp and blunt cowl lips.

M_0	*Cowl Lip*	M_{BC}	M_2	W_{C2}/W_{C2^*}	W_2/W_{cap}	p_{t2}/p_{t0}	IDC	IDR
1.664	Sharp	-	0.4755	0.9872	0.9729	0.9355	0.0862	0.1008
1.644	Blunt	-	0.4719	0.9851	0.9732	0.9379	0.0802	0.0940
0.20	Sharp	0.476	0.4767	0.9707	2.1018	0.8899	0.0448	0.1163
0.20	Blunt	0.468	0.4776	0.9723	2.1162	0.8946	0.0424	0.1174

4.5.2 Reducing the Inlet Flow Ratio

One approach examined for improving the inlet performance at the low-speed conditions was the reduction of the inlet flow ratio. Table 6 lists six simulations performed at M_0 = 0.2 for the inlet with the blunt cowl lip. The Mach number outflow boundary condition (M_{BC}) was used to establish the reduced inlet flow rate. As the inlet flow ratio was reduced, the total pressure recovery increased and IDC and IDR distortion descriptors decreased,

which indicated improvement. The variation in the performance metrics was essentially linear with respect to the inlet flow ratio. The stream thrust at the AIP was also calculated and that also varied linearly, which suggests a linear relationship between the flow rate and thrust of the propulsion system at $M_0 = 0.2$. Over the range of inlet flow ratios simulated, the stream thrust decreased by 10%. Reducing the inlet flow ratio is certainly an option for improving the inlet performance; however, a full understanding of the implications of reducing the inlet flow ratio on the thrust required for the aircraft requires a mission analysis, which was beyond the scope of this paper.

Table 6
Inlet performance at $M_0 = 0.2$ with a blunt cowl lip and variation of the inlet flow ratio.

M_0	*Cowl Lip*	M_{BC}	M_2	W_{C2}/W_{C2*}	W_2/W_{cap}	p_{t2}/p_{t0}	IDC	IDR
0.20	Blunt	0.476	0.4886	0.9840	2.1272	0.8884	0.0455	0.1244
0.20	Blunt	0.468	0.4776	0.9723	2.1162	0.8946	0.0424	0.1174
0.20	Blunt	0.450	0.4582	0.9462	2.0820	0.9044	0.0387	0.1066
0.20	Blunt	0.430	0.4369	0.9149	2.0347	0.9140	0.0347	0.0962
0.20	Blunt	0.410	0.4157	0.8821	1.9817	0.9233	0.0308	0.0866
0.20	Blunt	0.390	0.3945	0.8470	1.9214	0.9323	0.0302	0.0798

4.5.3 Deformation of the Cowl Lip

At the low-speed conditions of $M_0 < 0.4$, the inlet flow ratio is greater than one. The inlet streamtube contracts and the flow accelerates as it enters the inlet. One approach examined for improving the flow at these conditions was to deform the cowl lip so as to increase the capture area of the inlet. Increasing the capture area would reduce the speed and of flow and reduce the intensity of the vortices created as the flow sweeps past the scarfed leading edge of the inlet. This cowl lip deformation is envisioned as a variable-geometry feature of the inlet that would be employed during take-off, climb, and landing of the aircraft. At higher speeds, the inlet geometry would return to its non-deformed shape.

The deformation of the cowl lip involved a downward translation of the cowl lip profile at the symmetry plane and a transition of the cowl surfaces to match up with the non-deformed portions of the inlet. Figure 14 shows shaded images of the deformed inlet. The non-deformed inlet is shown as the black outline. The method of transition of the surfaces created some non-smooth portions of the surface, which show up in the shaded image of Fig. 14 near where the deformed cowl lip meets up with the non-deformed portion of the inlet. Also, the cowl exterior was changed with the deformation, but would not need to be changed in an actual inlet. These non-smooth surfaces and cowl exterior changes need to be fixed; however, they did not adversely impact the CFD simulations performed to assess the feasibility of deforming the cowl lip.

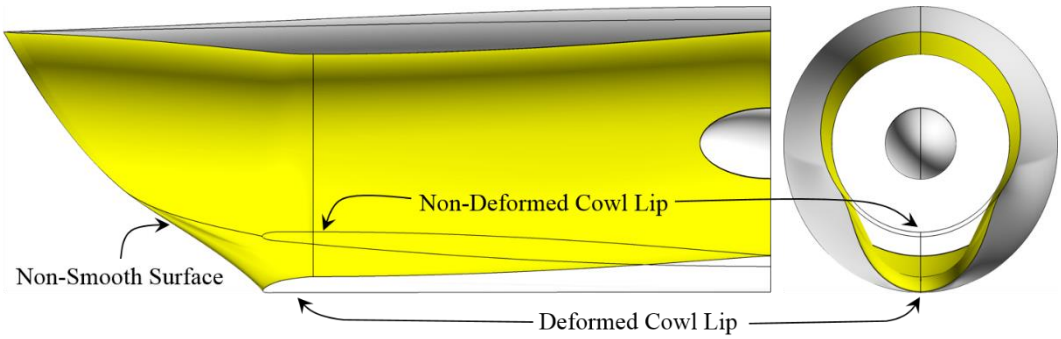

Figure 14. The inlet with the deformed cowl lip shown as shaded images and the non-deformed inlet shown as black outlines.

CFD simulations were performed for the inlets with the non-deformed and deformed cowl lips at $M_0 = 0.3$, which represented the low-speed conditions. The Mach number outflow boundary condition (M_{BC}) was used to set the inlet flow rate to near the AIP design corrected inlet flow rate. Figure 15 shows the images of the Mach number contours at axial stations through the inlets and the Mach number and total pressure recovery contours at the AIP. The Mach contours show that by increasing the cross-sectional area of the capture and throat, the local Mach numbers near the cowl lip were reduced to about Mach 0.6. The vortices that were created about the leading edge of the non-deformed inlet were almost eliminated in the deformed inlet. Table 7 lists the inlet performance metrics. The deformation of the cowl lip improved the total pressure recovery by over 6% and the distortion indices were reduced by almost half and were well within the distortion limits of Fig. 4. The distortion changed from being a hub distortion for the non-deformed inlet to a tip distortion for the deformed inlet.

This study only examined the aerodynamics of the internal flow as the cowl lip is deformed. The actual mechanics of performing such a deformation was beyond the scope of this paper, and is a separate engineering challenge in itself. The effect of the deformation on drag during low-speed operations also needs to be addressed in the context of its effect on the mission analysis.

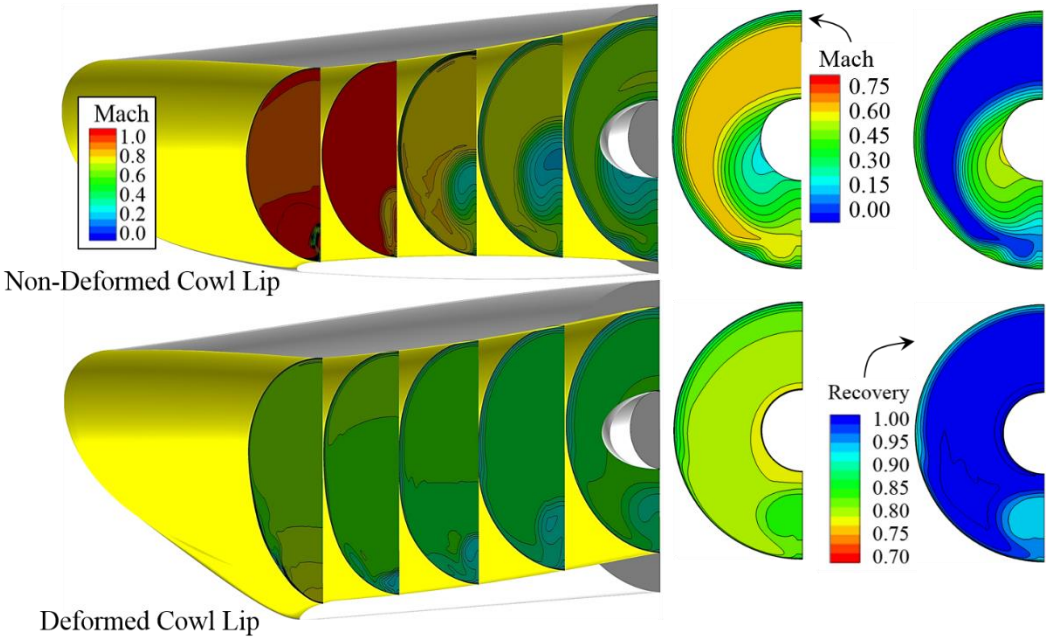

Figure 15. Mach number and AIP total pressure recovery contours for the inlets with non-deformed and deformed cowl lips at M_0 = 0.3.

Table 7
Inlet performance at M_0 = 0.3 for the inlets with non-deformed and deformed cowl lips.

Cowl Lip	M_2	W_{C2}/W_{C2*}	W_2/W_{cap}	p_{t2}/p_{t0}	IDC	IDR
Non-Deformed	0.4769	0.9828	1.5250	0.9287	0.0913	0.0524
Deformed	0.4685	0.9816	1.6181	0.9866	0.0276	0.0249

5.0 CONCLUSIONS

The aerodynamic performance of a streamline-traced, external-compression (STEX) inlet was examined for off-design conditions that included lower supersonic and subsonic Mach numbers, angles-of-attack, and angles-of-sideslip. The degradation of the inlet performance was of concern at negative angle-of-attack, angle-of-sideslip in excess of 3 degrees, and at low-speed conditions below M_0 = 0.6. A full understanding of the performance of the inlet at angle-of-attack and angle-of-sideslip needs to consider how the inlet would be integrated onto the aircraft. For a supersonic aircraft, the inlet would likely be highly-integrated with the fuselage or wing. Such integration may be able to take advantage of fuselage or wing shielding to limit the extent of incidence angles encountered by the inlet. Increasing the bluntness of the cowl lip improved the inlet performance at the design conditions and warrants consideration for the STEX inlet. Improvement of the inlet performance at the low-speed conditions was obtained by reducing the inlet flow ratio or by deforming the cowl lip to increase the capture and throat cross-sectional areas. The acceptability of reducing the inlet flow ratio requires an understanding of the mission analysis and an evaluation of the effect of lower inlet flow rate on the thrust of the propulsion system. The acceptability of deforming the cowl lip also requires an evaluation of pliable structures or variable-geometry, segmented inlet surfaces. Future studies will explore the use of auxiliary inlets at the low-speed conditions to allow alternative flow paths for air into the inlet.

ACKNOWLEDGMENTS

The author would like to acknowledge the support of the Commercial Supersonic Technology Project of the NASA Advanced Air Vehicles Program.

REFERENCES

[1] J W SLATER, "Methodology for the Design of Streamline-Traced, External-Compression Inlets," AIAA Paper 2014-3593, July 2014.

[2] S E OTTO, C J TREFNY, and J W SLATER, "Inward-Turning Streamline-Traced Inlet Design Method Low-Boom, Low-Drag Applications," *AIAA Journal of Propulsion and Power*, Vol. 32, No. 5, pp. 1178-1189, 2016.

[3] J W SLATER, "Enhanced Performance of Streamline-Traced External-Compression Supersonic Inlets," ISABE-Paper 2015-22049, October 2015.

[4] C M HEATH, J W SLATER, S K RALLABHANDI, "Inlet Trade Study for a Low-Boom Aircraft Demonstrator," AIAA Paper 2016-4050, June 2016.

[5] E BAYDAR, F K LU, J W SLATER, and C J TREFNY, "Vortex Generators in a Streamline-Traced, External-Compression Supersonic Inlet," AIAA Paper 2017-1383, January 2017.

[6] J W SLATER, "SUPIN: A Computational Tool for Supersonic Inlet Design," AIAA Paper 2016-0532, January 2016.

[7] D A YODER, "Wind-US User's Guide: Version 4.0," NASA TM 2016-219145, September 2016.

[8] M T MOORE, "Distortion Data Analysis," Report AFATPL-TR-72-111, February 1973.

[9] SOCIETY OF AUTOMOTIVE ENGINEERS (SAE), "Gas Turbine Engine Inlet Flow Distortion Guidelines," SAE ARP 1420, Rev. B, February 2002.

[10] W G STEENKEN, J G WILLIAMS, A J YUHAS, AND K R WALSH, "An Inlet Distortion Assessment during Aircraft Departures at High Angle of Attack for an F/A-18A Aircraft," NASA TM-104328, March 1997.

[11] G A GARZON, "Use of a Translating Cowl on a SSBJ for Improved Takeoff Performance," AIAA Paper 2007-0025, January 2007.